



**HAL**  
open science

**Physico-chemical characterization, Hirshfeld surface analysis and opto-electric properties of a new hybrid material: Tris (2-amino-5-chloropyridinium) hexachlorobismuthate(III)**

Zeineb Ouerghi, Thierry Roisnel, Ramzi Fezai, Riadh Kefi

► **To cite this version:**

Zeineb Ouerghi, Thierry Roisnel, Ramzi Fezai, Riadh Kefi. Physico-chemical characterization, Hirshfeld surface analysis and opto-electric properties of a new hybrid material: Tris (2-amino-5-chloropyridinium) hexachlorobismuthate(III). *Journal of Molecular Structure*, 2018, 1173, pp.439-447. 10.1016/j.molstruc.2018.05.084 . hal-01877852

**HAL Id: hal-01877852**

**<https://univ-rennes.hal.science/hal-01877852>**

Submitted on 20 Sep 2018

**HAL** is a multi-disciplinary open access archive for the deposit and dissemination of scientific research documents, whether they are published or not. The documents may come from teaching and research institutions in France or abroad, or from public or private research centers.

L'archive ouverte pluridisciplinaire **HAL**, est destinée au dépôt et à la diffusion de documents scientifiques de niveau recherche, publiés ou non, émanant des établissements d'enseignement et de recherche français ou étrangers, des laboratoires publics ou privés.

# Physico-chemical characterization, Hirshfeld surface analysis and opto-electric properties of a new hybrid material: Tris (2-amino-5-chloropyridinium) hexachlorobismuthate(III)

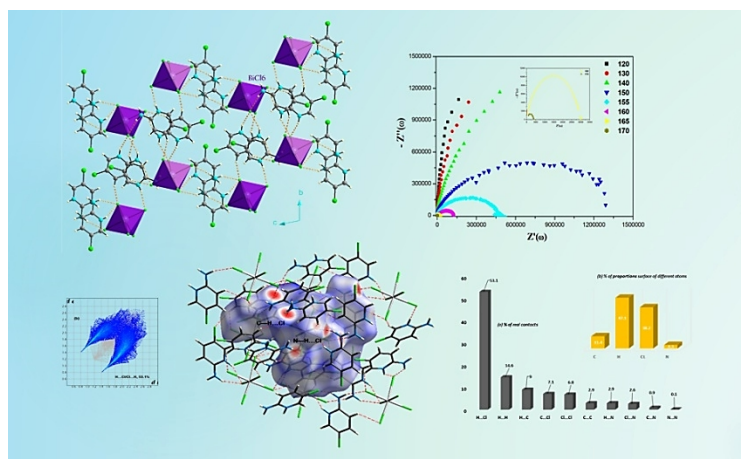
Zeineb Ouerghi<sup>[a]</sup>, Thierry Roisnel<sup>[b]</sup>, Ramzi Fezai<sup>[a]</sup> and Riadh Kefi<sup>[a]\*</sup>

<sup>[a]</sup> Laboratoire de Chimie des Matériaux, Université de Carthage, Faculté des Sciences de Bizerte, 7021, Zarzouna, Tunisia.

<sup>[b]</sup> Institut des Sciences Chimiques de Rennes UMR6226 CNRS, Université de Rennes 1, Campus de Beaulieu 35042 Rennes cedex, France.

\*Corresponding email: [Riadh.kefi@yahoo.com](mailto:Riadh.kefi@yahoo.com)

## Graphical abstract



## ABSTRACT:

One novel bismuth (III) hybrid compound with 2-amino-5-chloropyridine was prepared. The crystal was grown by slow evaporation method at room temperature. The structure was determined by single-crystal X-ray diffraction. It crystallizes in the triclinic space group  $P-1$ , with the following parameters:  $a = 7.5076(4) \text{ \AA}$ ,  $b = 12.3682(6) \text{ \AA}$ ,  $c = 15.1265(6) \text{ \AA}$  and  $\alpha = 98.893(2)^\circ$ ,  $\beta = 95.779(2)^\circ$ ,  $\gamma = 106.459(2)^\circ$  with  $Z = 2$  and  $V = 1315.26(11) \text{ \AA}^3$ . The structure was solved with a final  $R = 0.03$  for 5983 independent reflections. The crystal arrangement consists of  $[\text{BiCl}_6]^{3-}$  anions surrounded by  $[\text{C}_5\text{H}_6\text{ClN}_2]^+$  cations. Complex hydrogen bonding interactions between  $[\text{BiCl}_6]^{3-}$  and organic cations through  $\text{N}(\text{C})-\text{H}\cdots\text{Cl}$  hydrogen bonds form

a three-dimensional network. The crystal packing is stabilized by Cl $\cdots$ Cl interactions. Hirshfeld surface calculations were conducted to investigate intermolecular interactions, associated 2D fingerprint plots and enrichment ratio, revealing the quantitatively relative contribution of these interactions in the crystal packing. Thermal behavior was characterized by TG-DSC showing the decomposition of the compound at 180°C. Furthermore, Impedance spectroscopy study in the temperature range from 298 K to 443 K and in the frequency range between 5 and 13 MHz revealed that the temperature dependence of DC conductivity follows the Arrhenius law. Moreover, the frequency dependence of conductivity follows Jonscher's dynamical law. Nyquist plots ( $Z''$  versus  $Z'$ ) are well fitted to an equivalent circuit model which consists of a parallel combination of a bulk resistance  $R_b$  and constant phase elements CPE.

**Keywords:** hybrid material; hexachlorobismuthate; X-ray diffraction; Hirshfeld surface analysis; conductivity.

## Introduction

One of the most efficacious strategies to get novel functional materials with distinctive properties is to combine both organic and inorganic components into one material. They can be of great importance as they display a large variety of structures and a vast diversity of exceptional properties such as magnetic, optical and electrical properties. Metal-halides, in particular halogenobismuthates(III), with organic cations have been the subject of intense investigations due to their interesting photochemistry and photophysical properties caused by active lone pairs. Also, some special types of the anionic structure usually show ferroelectricity[1]. The discovery of this phenomenon in the group of halogenobismuthates(III), which can be described by the general formula  $R_aM_bX_{(3b+a)}$  (where

R stands for an organic cation, M = Bi(III) and X = Cl, Br, I), has increased the interest on this class of materials. The ferroelectricity appears in compounds involving different types of cations, such as small size alkylammonium (methyl-, dimethyl- and trimethylammonium) and unsubstituted heteroaromatic moieties (imidazolium and pyridinium)[2-3]. Furthermore, anionic species of bismuth halide have been observed to form variety of dimensionality[4]. In the case of chlorobismuthates, it can be octahedra, either isolated or connected with each other by bridging chlorine atoms forming more complicated arrays, like polyanionic one-, two- or three-dimensional nets, or sharing corners, edges or faces[5].

On the other hand, 2-aminopyridine and its derivatives constitute a class of compounds widely known for a long time and are continuing to generate considerable interest thanks to their promising application in several fields such as pharmaceutical, photo chemical, electro chemical and catalytic applications[6]. Especially, 2-Amino-5-chloropyridine, for its use as an intermediate in the pharmaceutical industry for the manufacture of Zopiclone, Zolpidem (hypnotic agents), and Alpidem (an anti-anxiety drug). It is also used as an intermediate in the agrochemical industry for the manufacture of Clodinafop[7].

Based on these facts, we have succeeded the synthesis of a new hybrid material based on chlorobismuthate(III) and we have reported in this manuscript its structural characterization, optical, thermal and dielectric properties.

## **2. Experimental**

### **2.1. Chemical preparation**

All reagents were obtained from commercial sources and used without purification. Bismuth(III) oxide (2.5 mmol, 1.16 g) and 2-amino-5-chloropyridine (2.5 mmol, 0.32 g) were dissolved in hydrochloric acid solution in presence of distilled water and ethanol in a stoichiometric ratio. The solution was stirred for 30 min at 50°C, and then, left with slow

evaporation at room temperature. Colourless prismatic crystals suitable for X-ray analysis were separated out from the solution after 5 days.

## 2.2. Investigation techniques

### 2.2.1. X-ray single crystal structural analysis

The X-ray intensity data was measured on D8 VENTURE Bruker AXS diffractometer equipped with, Mo-K $\alpha$  radiation ( $\lambda = 0.71073 \text{ \AA}$ ) at  $T = 150 \text{ K}$ . The structure was solved by dual-space algorithm using the SHELXT program [8], and then refined with full-matrix least-squares methods based on  $F^2$  (SHELXL) [9]. All non-hydrogen atoms were refined with anisotropic atomic displacement parameters. Except nitrogen linked hydrogen atoms that were introduced in the structural model through Fourier difference maps analysis, H atoms were finally included in their calculated positions and treated as riding on their parent atom with constrained thermal parameters. A final refinement on  $F^2$  with 5983 unique intensities and 299 parameters converged at  $\omega R(F^2) = 0.0805$  ( $R(F) = 0.0299$ ) for 5728 observed reflections with  $I > 2\sigma(I)$ . Crystal data, data collection parameters, and structure refinement details are given in Table 1.

### 2.2.2. Hirshfeld surface analysis

The Hirshfeld surface analysis of the title compound was performed using CrystalExplorer 3.1 [10] to figure out the normalized contact distance ( $d_{\text{norm}}$ ), which depends on contact distances to the closest atoms outside ( $d_e$ ) and inside ( $d_i$ ). The inter-contacts shorter than the sum of the van der Waals radii are highlighted on the  $d_{\text{norm}}$  surface in red which indicate the presence of possible hydrogen bonds while contacts closer in length or in the limit to the van der Waals radii are respectively colored blue and white. The two-dimensional fingerprint plots [11] were generated from the Hirshfeld surface by plotting the fraction of points on the surface as a function of the pair ( $d_i, d_e$ ) to summarize contact distances. The proportion of Hirshfeld surface contacts for the (X,Y) pair of elements is referred to  $C_{XY}$ . While, the proportion  $S_X$  of chemical type X on the molecular

surface is obtained according to the formula  $S_X = C_{XX} + \frac{1}{2} \sum_{Y \neq X} C_{XY}$ , the random contacts  $R_{XY}$  values are defined as if all contact types  $X \cdots Y$  in the crystal packing were equi-distributed between all chemical types and are obtained by probability products  $R_{XX} = S_X \cdot S_X$  and  $R_{XY} = 2S_X \cdot S_Y$ . All those formulas allowed us to calculate the enrichment ratios  $E_{XY} = C_{XY}/R_{XY}$  [12].

### 2.2.3. Physical measurements

FT-IR analysis was carried out at room temperature using NICOLET IR 200 FT-IR infrared spectrometer in the range of 4000–400  $\text{cm}^{-1}$ . Absorption spectrum was recorded, for the solid sample at room temperature with a Perkin Elmer Lambda 35 UV-Vis spectrophotometer equipped with an integrating sphere in the range of 200–700 nm. Emission and excitation spectra were recorded at room temperature for the solid sample with Perkin-Elmer LS55 spectrofluorometer. Simultaneous Thermogravimetry – Differential Scanning Calorimetry (TG-DSC) were performed using “NETZSCH STA 449F1” operating from 28°C up to 500°C temperature at an average heating rate of 5°C/min in Argon atmosphere using 5.50 mg of the sample.

### 2.2.4. Electrical measurements

The electrical measurements were performed using two electrode configurations on a polycrystalline sample, which in turn was pressed into pellets of 13 mm in diameter and 0.75 mm of thickness and with a signal amplitude of 0.5V. Electrical impedances were measured in the frequency range from 5 to 13 MHz and the temperature range between 293 and 443 K using a Hewlett–Packard HP 4192 Analyzer.

## 3. Results and discussion

### 3.1. Structure description

The asymmetric unit of the title compound consists of discrete  $\text{BiCl}_6^{3-}$  and three independent 2-amino-5-chloropyridinium cations as shown in Fig. 1. The Bi atom is six-fold coordinated

by chloride ions, forming an octahedral arrangement. Only the pyridinium N atom is protonated, while the amine group remains unprotonated, resulting in a charge of (+1) for the organic cation. Thus, to ensure charge equilibrium, the structure associates each hexachlorobismuthate(III) anions with three 2-amino-5-chloropyridinium cations. The Fig. 2 shows that the atomic arrangement of the title hybrid compound can be described as inorganic  $\text{BiCl}_6^{3-}$  interconnected from each other by the organic cations. Multiple hydrogen bonds connect those entities of the compound to form an infinite three-dimensional network. The crystal packing is influenced by  $\text{N-H}\cdots\text{Cl}$ , and  $\text{C-H}\cdots\text{Cl}$  hydrogen bonds. The  $(\text{N})\text{-H}\cdots\text{Cl}$  distances, varying between 2.34 and 2.69 Å (Table 2), are smaller than the sum of the Van der Waals radii of the chlorine and hydrogen atoms [ $r(\text{Cl}) + r(\text{H}) = 2.81$  Å]. Consequently, these values correspond well to strong hydrogen bonds. There are significantly short intermolecular  $\text{Cl}\cdots\text{Cl}$  interactions ( $\text{Cl1}\cdots\text{Cl3} = 3.759$  Å,  $\text{Cl1}\cdots\text{Cl2} = 3.523$  Å and  $\text{Cl2}\cdots\text{Cl3} = 3.375$  Å) (Fig. 3) in the structure leading to restrict the number of possible modes of packing.

The bismuth atom is octahedrally coordinated by chlorine atoms, with Bi-Cl distances ranging from 2.621(11) to 2.806(10) Å; their average bond length of 2.72 Å is significantly lower than the sum of van der Waals radii (3.83 Å), according to Pauling [13], and the Cl-Bi-Cl bond angles range from 82.49(3)° to 99.64(4)° (cis atoms) and 170.88(4)° to 177.86(3)° (trans atoms), with an average value of 90.01° and 173.9° respectively (Table 3). The different bond lengths, together with the bond angles distribution, give rise to a slight distortion of the  $[\text{BiCl}_6]^{3-}$  octahedra [14]; such a distortion is correlated not only to the primary deformation resulting from the stereochemical activity of Bi lone electron pair [15,16], but also to secondary deformations resulting from hydrogen bond interactions [17]. The involvement of any chlorine atom in hydrogen bonding results in a shift of the lone electron pair of the Bi atom in the direction of the H atom, which generally leads to an increase of the Bi-Cl

distance. In the present case such a behavior is observed for  $\text{Bi}_1\text{Cl}_{13}$ ,  $\text{Bi}_1\text{Cl}_{14}$  and  $\text{Bi}_1\text{Cl}_{15}$  bond lengths which are long with respect to the others.

In the organic entity, the N7-C4 bond [1.326(6) Å] is shorter than the N3-C4 [1.350(6) Å] and N3-C2 [1.365(6) Å] bonds, consistent with the iminium tautomer [18]. Moreover, the existence of the iminium tautomer is supported by the fact that the C4-C5 [1.415(6) Å] and C1-C6 [1.411(6) Å] bonds are longer than the C5-C6 [1.363(6) Å] and C1-C2 [1.345(6) Å] bonds. Similar features are also observed in other organic cations. However, previous study shows that a pyridinium cation always possesses an expanded angle of C-N-C in comparison with the parent pyridine [19]. It is worth noticing that all these geometrical characteristics are in good agreement with those of the related structure of the same cation,  $(\text{C}_5\text{H}_6\text{ClN}_2)_2[\text{ZnCl}_4]$  [20].

### 3.2. Hirshfeld surface analysis and enrichment ratio

To complete the study of the structural description, we have required the Hirshfeld surface analysis. In fact, it defines the space occupied by a molecule in the crystal by partitioning the electron density of the structure into molecular fragments. In addition, to gain more insights into the intermolecular interactions existing in the molecular crystal [21]. The Hirshfeld  $d_{\text{norm}}$  surface of  $[\text{C}_5\text{H}_6\text{N}_2\text{Cl}]_3\text{BiCl}_6$  is reported in Fig. 4. The recognition of the regions of particular importance to intermolecular interactions is given by mapping the normalized contact distance ( $d_{\text{norm}}$ ) expressed as:  $d_{\text{norm}} = (d_i - r_i^{\text{vdw}}) / r_i^{\text{vdw}} + (d_e - r_e^{\text{vdw}}) / r_e^{\text{vdw}}$ , where  $d_i$  and  $d_e$  are the distances to the nearest atoms inside and outside the surface while  $r_i^{\text{vdw}}$  and  $r_e^{\text{vdw}}$  are the van der Waals radii of the atoms [22]. The brighter and larger red spots observed in the  $d_{\text{norm}}$  refer to the shorter intermolecular contacts indicating the existence of hydrogen bonds: N—H $\cdots$ Cl as well as C—H $\cdots$ Cl in the crystal packing. Whereas, longer contacts are coloured in blue, and contacts around the vdW separation are coloured in white. Distances outside ( $d_e$ ) and inside ( $d_i$ ) mapped on the Hirshfeld surface are also used to

generate a fingerprint plots which consists in a two-dimensional summary of intermolecular interactions present between related molecules in the crystal structure. This decomposition provides a visualization containing implicit information of all intermolecular interactions as well as purely geometrical aspects like close contacts. This allows identification of prevailing interaction types such as, C...C or C...H interactions or hydrogen bonds [23, 24].

Fingerprint plots were calculated for the title compound for all phases. They are summarized in Fig. 5. The H...Cl contacts exhibit the characteristic shape of two “wings” at the top left and the bottom right of the Fingerprint plots (Fig. 5.b). In fact, they constitute the most important interactions in the crystal and their relative contribution extends to 53.1 % (indicated as red areas) due to the existence of N—H...Cl as well as C—H...Cl hydrogen bonds with distances down to 2.8 Å. In contrast, the H...H contacts are rather homogeneously extended over a large range of ( $d_i$ ,  $d_e$ )-pairs with an average contribution of 14.6 % (see Fig 6.a). They are generated between the organic cations inside the surface and the other molecules outside the Hirshfeld surface with distances around 3.3 Å. Besides, the C...H contacts are also broadly distributed with an accumulation comprising 9 % of the total surface and with distances down to 3.8 Å (Fig. 5.d). While, C...Cl and Cl...Cl contacts display relatively a sharp and acicular distribution with an average of 7.1 % and 6.8 % respectively (Fig 6.a). The intermolecular C...C and H...N interactions appear as short blue coloured patches with proportion of 2.9 %. In addition, Cl...N, C...N and N...N contacts are negligible and exhibit only 2.6 %; 0.9 % and 0.1 % respectively from the total surface area with  $(d_e+d_i) < 3.8$  Å. Furthermore, the compound doesn't show any  $\pi - \pi$  stacking interactions. In fact, the examination on the Hirshfeld surface doesn't reveal any adjacent red and blue triangles on the shape Index surface and no flat regions toward the bottom of both sides of the pyridinium moiety were detected on the curvedness surface (see Fig. 7).

we have also calculated the enrichment ratios to analyze the propensity of two chemical species to be in contact in the crystal packing. It is derived from the Hirshfeld surface and defined as the ratio between the proportion of actual contacts  $C_{XY}$  in the crystal (given by CrystalExplorer3.1) and the theoretical proportion of random contacts  $R_{XY}$  calculated from the corresponding  $S_X$  and  $S_Y$  proportions by the using of probability products.  $E_{XY}$  is superior than unity for a pair of elements with a larger propensity to form contacts, while enrichment value is lower than unity for a pair which tend to avoid contacts [25].

The enrichment ratios, actual and random contacts of the main intermolecular interactions in the compound are summarized in (Table 4). Most of contacts in the crystal structure are the  $H\cdots Cl$  type and they are well enriched with  $E_{HCl}=1.47$  which is due to the abundance of  $S_H=47.1\%$  and  $S_{Cl}=38.2\%$  in the total Hirshfeld surface area (see Fig. 5.b). Accordingly, the driving forces in the crystal packing are the electrostatic attraction of hydrogen bonds between  $BiCl_6$  anions and the pyridinium cations. In spite that the  $H\cdots H$  contacts represent the second most important surface interactions, they are moderately enriched. This is not surprising and can be explained to relatively their higher values of random contacts  $R_{HH}=22.18\%$  compared to the proportion of these contacts on the molecular surface  $C_{HH}=14.6\%$  (Fig.6.a; Table 4). The  $H\cdots C$  and  $C\cdots Cl$  intermolecular interactions are under-represented with  $E_{HC}=0.83$  and  $E_{CCl}=0.81$ ; while  $Cl\cdots Cl$  types are impoverished and marked by a low amount of enrichment ratio  $E_{ClCl}=0.46$ . In fact, the self-contacts  $X\cdots X$  are usually characterized by low  $E_{XX}$  ratios, considering that the same chemical atom type does not like to interact with itself because of the electrostatic repulsion between their charges of the same sign. Moreover,  $C\cdots C$  contacts take the most enrichment value corresponding to  $E_{CC}=2.23$  indicating that these types have an increased likelihood to form in the structure, which can be explained by the accumulation of aromatic nuclei in the crystalline stack,  $S_c=11.4\%$  (Fig.6.b). The  $H\cdots N$  and  $Cl\cdots N$  contacts are characterized by favored enrichment ratios equivalent or close to the unity as well as for

C...N and N...N contacts:  $E_{NH} = 0.93$ ;  $E_{CIN} = 1.03$   $E_{CN} = 1.19$  and  $E_{NN} = 0.91$ . These are due to the negligible amount of random contacts in the crystal with  $R_{HN} = 3.10$   $R_{CIN} = 2.52$   $R_{CN} = 0.75$  and  $R_{NN} = 0.10$  (Table 4).

### 3. 3. IR Spectroscopy

IR spectroscopy is an efficient method to confirm the functional groups present in the crystal and to study the structural consequences such as in plane or out of plane vibrations [26]. Herein, we have discussed the vibrational analyses of the compound and tried to give most precise assignment of the observed bands. FT-IR spectrum is shown in (Fig. 8). The strong and broad band, formed by overlapped peaks between 3500-2800  $\text{cm}^{-1}$  region, corresponds to the valence vibrations of N—H and C—H groups interconnected by a system of hydrogen bonds in the crystal. In fact, the broadening of the band is caused by hydrogen bonding interactions which influence the frequency as well as the intensity of the peak [27]. The observed band at 1672  $\text{cm}^{-1}$  can be assigned to the C=N group. In addition, the N—H bending vibration appears at 1626  $\text{cm}^{-1}$ . The C=C aromatic stretches are predicted at 1547 and 1455  $\text{cm}^{-1}$  [28]. Moreover, the band located at 1324  $\text{cm}^{-1}$  can be assigned to C—N or C—NH<sub>2</sub> stretching vibrations [29]. The group of vibrations in approximately 1100-600  $\text{cm}^{-1}$  range can be attributed to the out of plane bending modes of C—H, C—C, C—Cl and C—N groups [30]. Furthermore, the C—Cl stretching mode occurs at 662  $\text{cm}^{-1}$ . Consequently, the presence of functional groups of the cation was proved and agreed with the literature data.

### 3.4. Optical properties

The solid-state UV-Visible spectrum of  $[\text{C}_5\text{H}_6\text{ClN}_2]_3\text{BiCl}_6$  was given in (Figure 9.a). The crystal exhibits two distinct absorption bands. The first band around 271 nm (4.57 eV) corresponds to  $\pi - \pi^*$  transitions, which are relative to the aromatic conjugation in the cations. The second band at 350 nm (3.54 eV) can be attributed to the charge transfer maxima of chlorobismuthate(III) anions [31, 32].

The energy band gap value is useful to determine the chemical reactivity and kinetic stability of the molecule [28]. It refers to the energy difference between the valence band and the conduction band of a solid material. In other words, it represents the minimum energy that is required to excite an electron up to a state in the conduction band where it can participate in conduction. The evaluated band gap of our compound was found to be 3.2 eV according to the Tauc plot method (see Fig. 9.b) which indicates that the crystal can have dielectric behavior to induce polarization when powerful radiation is incident on the material [33]. This value was obtained from the formula:  $(\alpha h\nu)^{1/n} = A(h\nu - E_g)$  with  $n = 1/2$  for direct allowed transitions, where  $h$  is Planck's constant,  $\nu$  is the photon's frequency,  $\alpha$  is the absorption coefficient,  $E_g$  is the band gap, and  $A$  is a proportionality constant [34].

To explore the potential application as luminescent material, solid state fluorescent properties for the title crystal was studied. The figure 10 shows the simultaneous emission (a) and excitation (b) luminescence spectra. The emission spectrum recorded at an excitation wavelength of 340 nm exhibits three emission peaks in the visible region of the electromagnetic spectrum. The broad band observed at 425 nm followed by less intense bands at 453 and 484 nm may be attributed to intra ligand  $\pi^* - \pi$  transition of the pyridinium part and ligand to metal charge transfer transition within the chlorobismuthate inorganic part [35, 36]. The excitation spectrum which reports the variation of the intensity of the emission band at 425 nm as a function of excitation wavelengths shows two distinct bands, at 307 and 332 nm, well confirming the selected region of the excitation wavelength.

### 3.5. Thermal behavior

To study the thermal stability and decomposition of  $[\text{C}_5\text{H}_6\text{ClN}_2]_3\text{BiCl}_6$  crystals we have recourse to TG-DSC analysis. Fig. 11 shows that the studied compound remains stable up to 145°C where we note in the DSC curve a change in the baseline at 150°C corresponding to a phase transition. Further heating gives rise to two endothermic peaks in the temperature range

from 160 to 260°C. These thermal phenomena are accompanied by the first weight loss, in the TG curve, of approximately 50.74%. Therefore, the first late peak at 190 °C corresponds to the melting point of the compound, the second one, at 220°C, which is wide and more intense can be attributed to the decomposition of the organic part of the heated sample (percentage of the three cations = 47.94%). Besides, the second mass change take place between 260° and 300°C with an experimental weight loss of 42.85%, in coincidence with the DSC results exhibiting an endothermic peak at 300 °C, can be attributed to the decomposition and the sublimation of the rest of the compound and the release of probably volatile substances such as Cl<sub>2</sub> molecules. These results are confirmed by heating a sample of this hybrid bismuth on a Kofler bench showing clearly the melt of the tested material and the release of the gas. This study suggests that the crystal can be used for applications such as optoelectronic devices below 160°C temperature.

### **3.6. Electrical properties**

#### *3.6.1. Impedance analysis*

The Nyquist diagram (Imaginary part versus real part of the impedance data:  $Z''$  versus  $Z'$ ) of the studied compound at different temperatures is shown in Fig. 12. The well-defined semicircles either passing through or close to the origin were obtained for  $393\text{K} \leq T \leq 443\text{K}$ . As temperature increases, these circles become tediously smaller indicating an activated thermal conduction mechanism. The equivalent electrical circuit of this sample could be regarded as parallel combination of a bulk resistance  $R_b$  and constant phase element CPE.

We report in Figures 13 (a) and (b) the real and imaginary parts of impedance  $Z'$  and  $Z''$ , respectively, as a function of frequency at different temperatures. The magnitude of  $Z'$  decreases with the increasing of both temperature and frequency and the AC conductivity increase. The phenomenon revealed that the as-synthesized material behaves like semi conducting material.  $Z''$  increased with frequency until reaching a maximum peak ( $Z''_{\text{max}}$ )

then decreased with the increasing frequency. Furthermore,  $Z''_{max}$  values decrease with the increasing temperature and shifts towards higher frequency side indicating a single relaxation time.

### 3.6.2. Modulus analysis

The complex modulus formalism has been used in the analysis of the electrical properties because it gives information about the relaxation mechanism. The electric modulus data are calculated from the real and imaginary parts of the measured impedance data and the pellet dimensions using the following equations:

$$M' = -\omega C_0 Z''; M'' = \omega C_0 Z' \text{ where } C_0 = \epsilon_0 S/e.$$

The frequency dependence of the real and imaginary part  $M'$  &  $M''$  of the title material at different temperatures are given respectively in Figures 14 (a) and (b). At low frequencies,  $M'$  approaches nearly zero at all temperatures suggesting the suppression of the electrode polarization. At high frequencies,  $M'$  displaying a maximum value corresponding to  $M_\infty$  due to relaxation process. For  $M''$  variation, it is observed that the shape of the curve is asymmetric with a constant  $M''_{max}$  value, to which a characteristic relaxation rate can be associated, and the peak frequency shifts towards the higher frequency region.

### 3.6.3. Conductivity study

The thermal evolution of the specific conductivity ( $\ln(\sigma T)$  versus  $1000/T$ ) is reported in Fig. 15, indicating an Arrhenius-type behavior ( $\sigma T = A \exp(-E_a/KT)$ ). The bulk conductivity is calculated by the following formula:  $\sigma = K_c/R$ ;  $K_c = e/S$  (where  $e$  is the thickness of the sample and  $S$  is the electrode surface area). Two regions associated with two activation energies are observed separated at  $T = 423$  K. Thus, following the Arrhenius law, the obtained activation energies are  $E_{a1} = 9.41$  eV in region I and  $E_{a2} = 2.02$  eV in region II. These observations suggested that the conductivity is caused by temperature increase of the protons hoping

motion. These results are in good agreement with the thermal analysis showing a phase transition at 418K.

The frequency–temperature dependence of AC conductivity for the studied sample is given in Fig.16. This figure shows two regions; the first one is a plateau, at low frequencies, which corresponds to direct current conductivity  $\sigma_{dc}$  and the second region is a dispersion characterized by an increase of the  $\sigma_{AC}$  values with the increase in frequency, which is a characteristic of  $\omega^n$ . This phenomenon is given by universal power law governed by the relation [37]:  $\sigma(\omega) = \sigma_{dc} + A\omega^n$ ; where  $\sigma_{dc}$  is the frequency independent dc (or low-frequency) conductivity,  $\omega$  the angular frequency of measurement, A and n are fitting parameters. Such behavior has been observed with other organic-inorganic hybrid materials [38,39]. The increase of temperature leads to an increase of  $\sigma_{AC}$  values and the plateau characterizing  $\sigma_{dc}$  conductivity becomes wider and thus the frequency characteristic of the beginning of the dispersion ( $\omega_H$ ) is shifted towards higher frequencies.

## Conclusion

In summary we have presented the synthesis and physicochemical characterization of the new compound  $[C_5H_6ClN_2]_3BiCl_6$ . The crystal packing consists of  $[BiCl_6]^{3-}$  anions surrounded by  $[C_5H_6ClN_2]^+$  cations and is stabilized by hydrogen bonding and van der Waals interactions creating a three-dimensional network between  $[BiCl_6]^{3-}$  and organic cations. Hirshfeld surface allowed us to investigate the stabilization of the crystal packing and to quantify the propensity of the intermolecular interactions to form the supramolecular assembly. The presence of functional groups of the cation was proved by IR. The optical properties were examined by optical absorption and fluorescence measurements. The electrical behavior of the title compound was studied as a function of temperature and frequency. The AC conductivity was found to obey the universal power law. The analysis of the temperature variation of

M" indicates that the observed relaxation process is thermally activated. Moreover, the temperature dependence of conductivity was analyzed using the Arrhenius approach.

### **Supplementary data**

Crystallographic data of the structure have been deposited in the Cambridge Crystallographic data center CCDC 1836728. These data can be obtained free of charge via [www.ccdc.cam.ac.uk/data\\_request/cif](http://www.ccdc.cam.ac.uk/data_request/cif).

### **Acknowledgements**

This work was supported by the Tunisian National Ministry of Higher Education and Scientific Research.

**References**

- [1] Y. J. Wang and L. Xu. *J. Mol. Struct.* 875 (2008) 570–576.
- [2] I. Płowas, A. Białońska, G. Bator, R. Jakubas, W. Medycki and J. Baran. *Eur. J. Inorg. Chem.* (2012) 636–646.
- [3] A. Piecha, A. Gagor, M. Weclawik, R. Jakubas and W. Medycki. *J. Mater. Res. Bull.* 48 (2013) 151–157.
- [4] D. Fredja, C. B. Hassena, S. Elleuchb, H. Fekib, N. C. Boudjadac, T. Mhiri and M. Boujelbene. *J. Mater. Res. Bull.* 85 (2017) 23–29.
- [5] B. Zarychta, M. Bujak and J. Zaleski. *Z. Naturforsch.* 59b (2004) 1029–1034.
- [6] T. Jayanalina, G. Rajarajan, K. Boopathi and K. Sreevani. *J. Cryst. Growth.* 426 (2015) 9–14.
- [7] K. Thanigaimani, N. C. Khalib, E. Temel, S. Arshad, I. A. Razak. *J. Mol. Struct.* 1099 (2015) 246–256
- [8] G. M. Sheldrick, *Acta Cryst.* A71 (2015) 3–8.
- [9] G. M. Sheldrick, *Acta Cryst.* C71 (2015) 3–8.
- [10] S. K. Wolff, D. J. Grimwood, J. J. McKinnon, M. J. Turner, D. Jayatilaka, M. A. Spackman, *CrystalExplorer*. University of Western Australia, Perth, 2012.
- [11] J. J. McKinnon, D. Jayatilaka and M. A. Spackman. *Chem. Commun.* (2007) 3814–3816.
- [12] C. Jelsch, K. Ejsmont and L. Huder, *IUCrJ.* 1 (2014) 119–128.
- [13] L. Pauling, *The Nature of Chemical Bond*, Cornell University, Press, Ithaca, NY, USA, 1960.
- [14] A. V. Polishchuk, A. V. Gerasimenko, K. A. Gayvoronskaya and E. T. Karaseva, *Acta Crystallogr.* E64 (2000) m931–m932.
- [15] S. Chaabouni, S. Kamoun and J. Jaud. *J. Chem. Crystallogr.* 28 (1998) 209–212.
- [16] X. Wang and F. Liebau. *Acta Crystallogr.* B 52 (1996) 7–15.

- [17] J. Zaleski and A. Pietraszko. *Acta. Crystallogr. B* 52 (1996) 287–295.
- [18] Z. Min Jin, Y. Jiang Pan, M. Lin Hu and S. Liang. *J. Chem. Crystallogr.* 31(2001)191–195.
- [19] Z-M. Jin, B. Tu, L. He, M-L. Huc and J-W. Zou. *Acta Cryst.* C61(2005) 197–199.
- [20] R. Kefi, E. Jeanneau, F. Lefebvre and C. Ben Nasr. *Acta Cryst.*E71 (2015) 555–557.
- [21] S. Shit, C. Marschner and S. Mitra, *Acta Chim. Slov.* 63 (2016) 129–137.
- [22] J. J. McKinnon, D. Jayatilaka and M. A. Spackman, *Chem. Commun.* 37 (2007) 3814–3816.
- [23] M. Klues and G. Witte. *CrystEngComm.* 20 (2018) 63–74.
- [24] B. Schatschneider, J. Phelps and S. Jezowski. *CrystEngComm.* 13 (2011) 7216–7223.
- [25] A. Saeed, M. Bolte, M.F. Erben and H. Pérez, *CrystEngComm.* 17 (2015) 7551–7563
- [26] K. Thanigaimani, N. C. Khalib, E. Temel, S. Arshad and I. A. Razak. *J. Mol. Struct.* 1099 (2015) 246-256.
- [27] T. Suthan, N.P. Rajesh, C.K. Mahadevan and G. Bhagavannarayana, *Mater. Chem. Phys.* 129 (2011) 433– 438.
- [28] B. Babu, J. Chandrasekaran, B. Mohanbabu, Y. Matsushita and M. Saravanakumar, *RSC Adv.* 6 (2016) 110884–110897.
- [29] S. L. Srivastava, R. K. Goel and R. ohitashava, *J. Chim. Phys.* 75 (1978) 1091–1095.
- [30] R. Kefi, M.ElGlaoui, M. Zeller, F. Lefebvre and C. Ben Nasr. *Elixir Appl. Chem.* 42 (2012) 6124–6130.
- [31] A. Vogler, A. Paukner and H. Kunkely, *J. Coord. Chem. Rev.* 97 (1990) 285–297.
- [32] A. Vogler and H. Nikol, *J. Pure Appl. Chem.* 1311 (1992) 64–9.
- [33] R. Thirumurugan, B. Babu, K. Anitha and J. Chandrasekaran. *Spectrochim. Acta, Part A.* 140 (2015) 44–53.

- [34] B.D. Viezbicke, S. Patel, B.E. Davis and D.P. Birnie, *Phys. Status Solidi B* (2015) 1–11.
- [35] S. A. Adonin, M. I. Rakhmanova, D. G. Samsonenko, M. N. Sokolov and V. P. Fedin. *Inorg. Chim. Acta* (2016) 232–235.
- [36] W. Trigui, A. Oueslati, F. Hlel and A. Bulou. *J. Mol. Struct.* 1106 (2016) 19–29.
- [37] A. Ben Rhaiem, N. Zouari, K. Guidara, M. Gargouri, and A. Daoud. *J. Alloy. Compd.* 392 (2005) 68–71.
- [38] K. Karoui, A. Ben Rhaiem, F. Hlel, M. Arous, and K. Guidara. *Mater. Chem. Phys.* 133 (2012) 1–7.
- [39] A. Ben Rhaiem, F. Hlel, K. Guidara, and M. Gargouri. *J. Alloy. Compd.* 463 (2008) 440–445.

**Table captions**

**Table 1.** Crystallographic data and structure refinement parameters for the crystal.

**Table 2.** Hydrogen bonding parameters(Å, °).

**Table 3.** Selected bond distances and angles (Å, °) in  $3(\text{C}_5\text{H}_6\text{ClN}_2)\cdot\text{BiCl}_6$ .

**Table 4.** Hirshfeld contact surfaces, derived random contacts and enrichment ratios of different species present on the molecular surface in the compound.

**Table 1**

<b><i>Crystal data</i></b>	
Chemical formula	3(C <sub>5</sub> H <sub>6</sub> ClN <sub>2</sub> )·BiCl <sub>6</sub>
$M_r$	810.38
Crystal system, space group	Triclinic, <i>P-1</i>
Temperature (K)	150
$a, b, c$ (Å)	7.5076(4), 12.3682(6), 15.1265(6)
$\alpha, \beta, \gamma$ (°)	98.893(2), 95.779(2), 106.459(2)
$V$ (Å <sup>3</sup> )	1315.26(11)
$Z$	2
Radiation type	Mo $K\alpha$
$\mu$ (mm <sup>-1</sup> )	7.63
Crystal size (mm)	0.42 × 0.31 × 0.13
<b><i>Data collection</i></b>	
Diffractometer	D8 VENTURE Bruker AXS
$T_{\min}, T_{\max}$	0.134, 0.371
No. of measured, independent and observed [ $I > 2\sigma(I)$ ] reflections	29578, 5983, 5728
$R_{\text{int}}$	0.050
$(\sin \theta/\lambda)_{\text{max}}$ (Å <sup>-1</sup> )	0.649
<b><i>Refinement</i></b>	
$R[F^2 > 2\sigma(F^2)], wR(F^2), S$	0.030, 0.080, 1.01
No. of reflections	5983
No. of parameters	299
No. of restraints	6
$\Delta\rho_{\text{max}}, \Delta\rho_{\text{min}}$ (e Å <sup>-3</sup> )	2.60, -4.00

Table 2

$D-H\cdots A$	$D-H$	$H\cdots A$	$D\cdots A$	$D-H\cdots A$
N3—H3 $\cdots$ Cl12 <sup>i</sup>	0.86	2.34	3.184(4)	166.0
C6—H6 $\cdots$ Cl14 <sup>ii</sup>	0.95	2.75	3.563(4)	143.5
N7—H7B $\cdots$ Cl16	0.88(2)	2.52(3)	3.351(4)	159(5)
N13—H13 $\cdots$ Cl11	0.84	2.40	3.195(4)	157.8
N17—H17A $\cdots$ Cl11	0.87(2)	2.45(3)	3.246(4)	152(5)
N17—H17B $\cdots$ Cl15 <sup>iii</sup>	0.87(2)	2.45(2)	3.298(4)	165(5)
N23—H23 $\cdots$ Cl16 <sup>iv</sup>	0.90	2.55	3.319(4)	143.8
C25—H25 $\cdots$ Cl12 <sup>v</sup>	0.95	2.62	3.472(4)	149.5
C26—H26 $\cdots$ Cl11 <sup>vi</sup>	0.95	2.76	3.616(4)	150.3
N27—H27A $\cdots$ Cl16 <sup>iv</sup>	0.88(2)	2.55(4)	3.333(4)	149(5)
N27—H27B $\cdots$ Cl12 <sup>v</sup>	0.88(2)	2.69(3)	3.486(4)	151(5)

Symmetry codes : (i)  $-x+1, -y, -z+1$ ; (ii)  $-x+2, -y+1, -z+1$ ; (iii)  $-x+1, -y, -z$ ; (iv)  $x-1, y, z$ ; (v)  $-x+1, -y+1, -z+1$ ; (vi)  $x, y+1, z$ .

Table 3

C1—C2	1.345(6)	C21—C26	1.409(6)
C1—C6	1.411(6)	C22—N23	1.367(5)
C2—N3	1.364(6)	N23—C24	1.355(5)
C4—C5	1.415(6)	C24—N27	1.335(6)
C4—N7	1.326(6)	C24—C25	1.412(6)
C5—C6	1.363(6)	C25—C26	1.364(6)
N3—C4	1.350(6)	C14—N17	1.333(6)
Cl2—C11	1.725(4)	C14—C15	1.418(6)
C11—C12	1.356(6)	C15—C16	1.361(6)
C11—C16	1.404(6)	Bi1—Cl14	2.6215(11)
C12—N13	1.362(6)	Bi1—Cl13	2.6502(10)
N13—C14	1.344(6)	Bi1—Cl15	2.6918(10)
Cl1—C1	1.737(4)	Bi1—Cl12	2.7436(10)
Cl3—C21	1.733(4)	Bi1—Cl11	2.7750(10)
C21—C22	1.354(6)	Bi1—Cl16	2.8067(10)
C2—C1—C6	120.5(4)	N7—C4—N3	119.6(4)
C2—C1—Cl1	119.2(3)	N7—C4—C5	122.8(4)
C6—C1—Cl1	120.2(3)	N13—C14—C15	117.9(4)
C1—C2—N3	118.9(4)	N17—C14—N13	119.7(4)
C4—N3—C2	123.6(4)	N23—C24—C25	117.5(4)
C5—C6—C1	119.5(4)	N27—C24—N23	119.2(4)
C6—C5—C4	119.8(4)	N27—C24—C25	123.3(4)
C11—C12—N13	118.7(4)	Cl14—Bi1—Cl13	99.64(4)
C12—C11—Cl2	119.8(3)	Cl14—Bi1—Cl15	91.47(4)
C12—C11—C16	120.1(4)	Cl13—Bi1—Cl15	92.04(3)
C15—C16—C11	120.1(4)	Cl14—Bi1—Cl12	88.30(3)
C14—N13—C12	123.7(4)	Cl13—Bi1—Cl12	90.09(3)
C16—C15—C14	119.4(4)	Cl15—Bi1—Cl12	177.86(3)
C16—C11—Cl2	120.1(3)	Cl14—Bi1—Cl11	170.88(4)
C21—C22—N23	119.5(4)	Cl13—Bi1—Cl11	88.47(3)
C22—C21—Cl3	120.2(3)	Cl15—Bi1—Cl11	92.38(3)
C22—C21—C26	119.5(4)	Cl12—Bi1—Cl11	87.54(3)

C26—C21—C13	120.2(3)	C114—Bi1—C116	84.98(3)
C24—N23—C22	123.2(4)	C113—Bi1—C116	172.96(3)
C25—C26—C21	120.1(4)	C115—Bi1—C116	82.49(3)
C26—C25—C24	120.1(4)	C112—Bi1—C116	95.38(3)
N3—C4—C5	117.7(4)	C111—Bi1—C116	87.34(3)

Table 4

	<i>Contacts (C, %)</i>	<i>Random contacts (R, %)</i>	<i>Enrichment (E)</i>
H···Cl	53.1	35.98	1.47
H···H	14.6	22.18	0.65
H···C	9	10.73	0.83
C···Cl	7.1	8.70	0.81
Cl···Cl	6.8	14.59	0.46
C···C	2.9	1.29	2.23
H···N	2.9	3.10	0.93
Cl···N	2.6	2.52	1.03
C···N	0.9	0.75	1.19
N···N	0.1	0.10	0.91

**Figure captions list**

**Fig. 1.** Asymmetric unit of  $[\text{C}_5\text{H}_6\text{ClN}_2]_3\text{BiCl}_6$ . Thermal ellipsoids are shown at 50% probability.

**Fig. 2.** Projection of the structure of  $[\text{C}_5\text{H}_6\text{ClN}_2]_3\text{BiCl}_6$  along the b axis. A polyhedral representation is used for the  $\text{BiCl}_6$  octahedron.

**Fig. 3.** A view of  $\text{Cl}\cdots\text{Cl}$  contacts in the compound  $[\text{C}_5\text{H}_6\text{ClN}_2]_3\text{BiCl}_6$ .

**Fig. 4.** Hirshfeld surfaces mapped with  $d_{\text{norm}}$  for the title compound (the surface is shown as transparent to allow visualization of the orientation of the asymmetric unit), showing hydrogen bonds through  $\text{N}-\text{H}\cdots\text{Cl}$  and  $\text{C}-\text{H}\cdots\text{Cl}$  with neighbouring molecules.

**Fig. 5.** Hirshfeld surface mapped with shape index in the middle and curvedness in the right for the title compound.

**Fig. 6.** The 2D fingerprint plots of  $[\text{C}_5\text{H}_6\text{ClN}_2]_3\text{BiCl}_6$  arising from the different intermolecular contacts are clearly shown, where  $d_e$  and  $d_i$  are the distances to the nearest exterior and interior atoms to the surface.

**Fig. 7.** Histogram of different percentages of real contacts (a) and proportion surface of different atoms (b).

**Fig. 8.** IR spectrum of  $[\text{C}_5\text{H}_6\text{ClN}_2]_3\text{BiCl}_6$ .

**Fig. 9.** Solid-state UV-Vis spectrum (a) of  $(\text{C}_5\text{H}_6\text{ClN}_2)_3[\text{BiCl}_6]\cdot\text{H}_2\text{O}$  and the energy gap (b) according to the Tauc model.

**Fig. 10.** View of emission (a) and excitation (b) spectra of the compound in the solid state at room temperature.

**Fig. 11.** TG-DSC curve of  $[\text{C}_5\text{H}_6\text{ClN}_2]_3\text{BiCl}_6$ .

**Fig.12.** Complex impedance diagrams ( $-Z''$  vs  $Z'$ ) for  $[\text{C}_5\text{H}_6\text{ClN}_2]_3\text{BiCl}_6$  at various temperatures.

**Fig.13.** Plots of the real and imaginary parts of impedance  $Z'$  (a) and  $Z''$  (b) vs.  $\log(f)$  of  $[\text{C}_5\text{H}_6\text{ClN}_2]_3\text{BiCl}_6$  at various temperatures.

**Fig.14.** Variation of the real  $M'$  (a) and imaginary parts  $M''$  (b) of the electric modulus as a function of the frequency at various temperatures in  $[\text{C}_5\text{H}_6\text{ClN}_2]_3\text{BiCl}_6$ .

**Fig.15.** The frequency dependence of the AC conductivity at various temperatures in the structure of  $[\text{C}_5\text{H}_6\text{ClN}_2]_3\text{BiCl}_6$ .

**Fig.16.** Variation of the  $\ln(\sigma T)$  versus  $1000/T$  for the  $[\text{C}_5\text{H}_6\text{ClN}_2]_3\text{BiCl}_6$  compound.

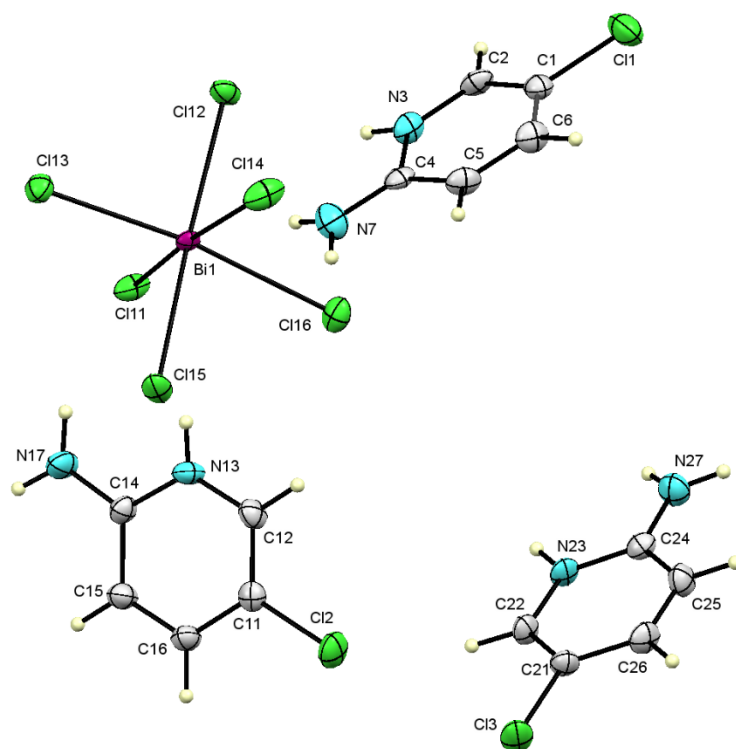


Fig. 1

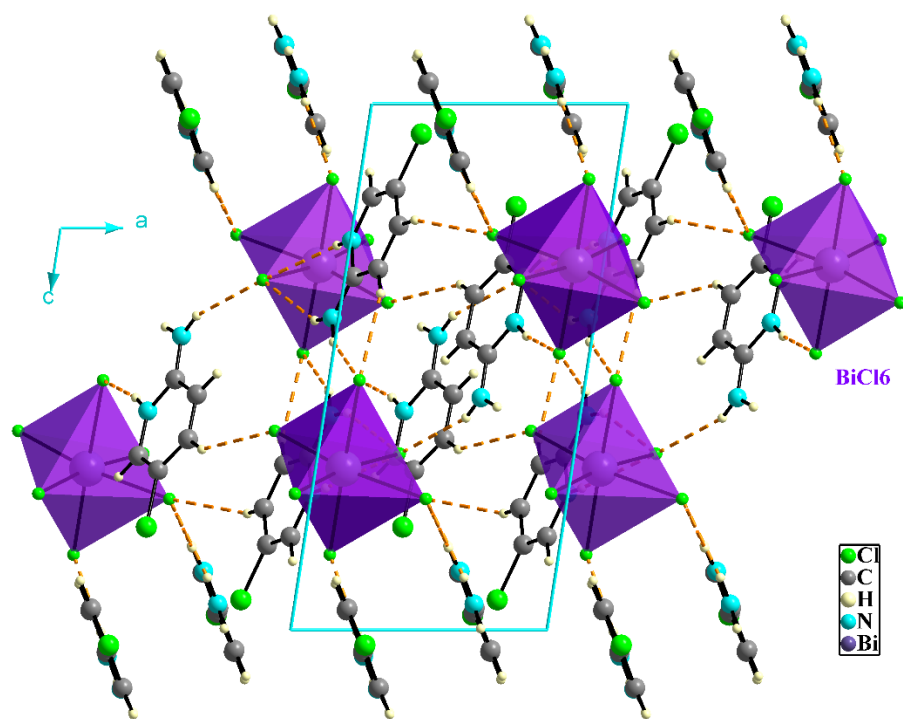


Fig. 2

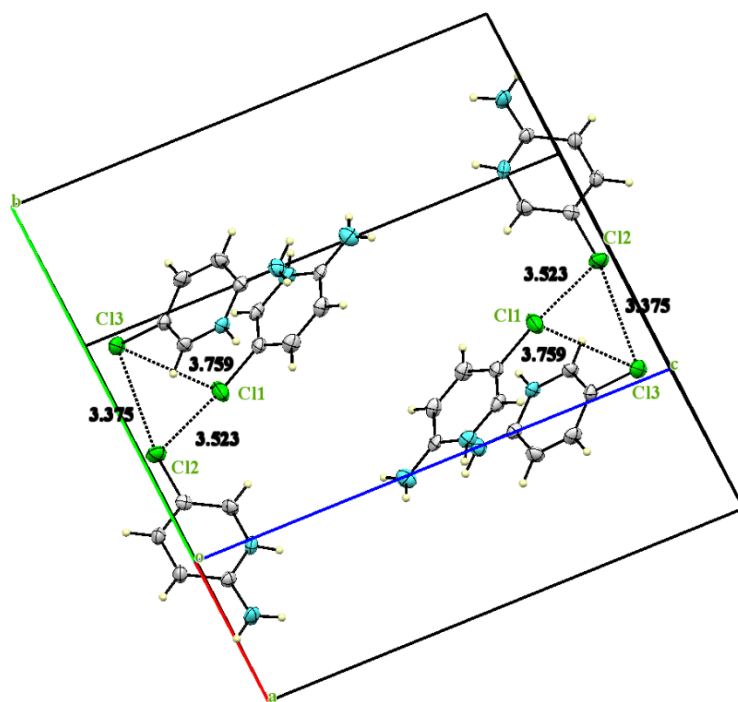


Fig.3

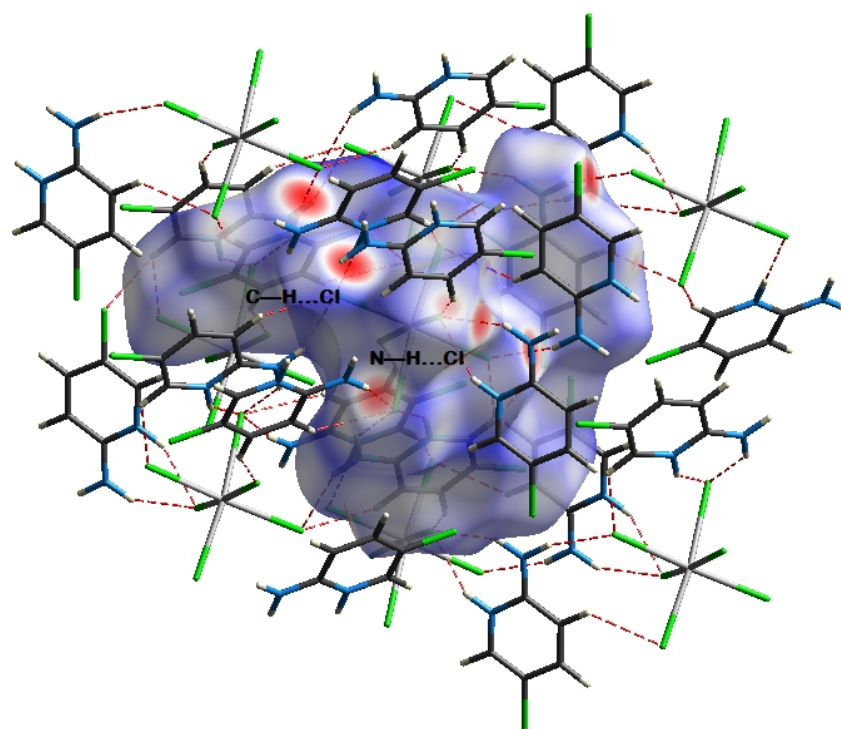


Fig.4

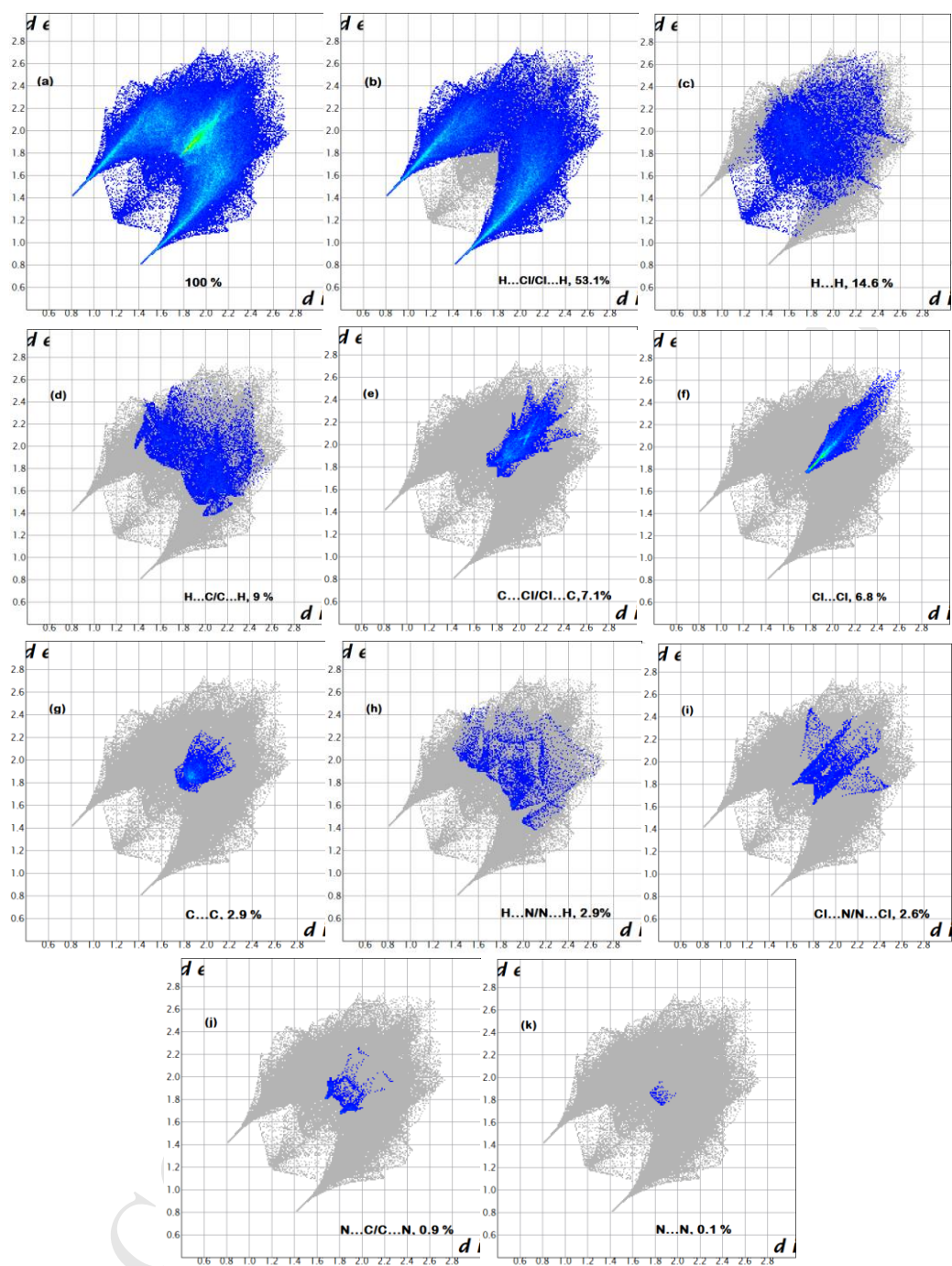


Fig.5

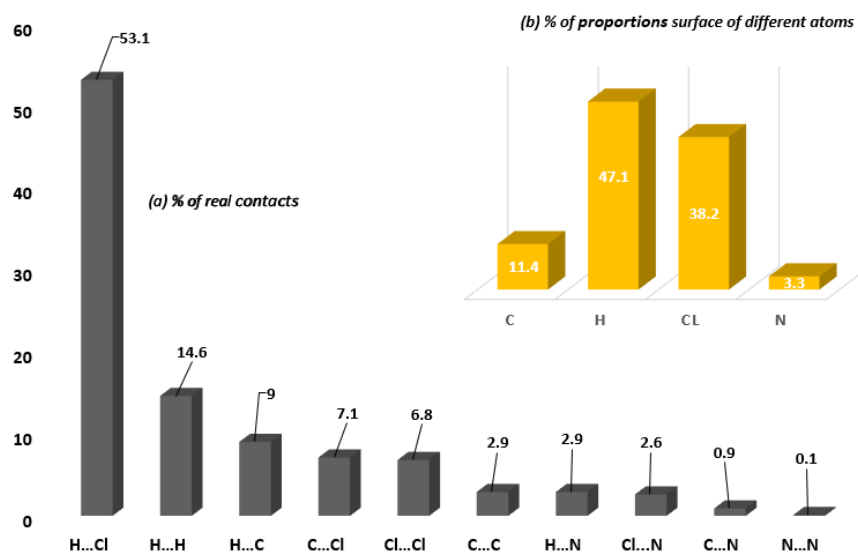


Fig. 6

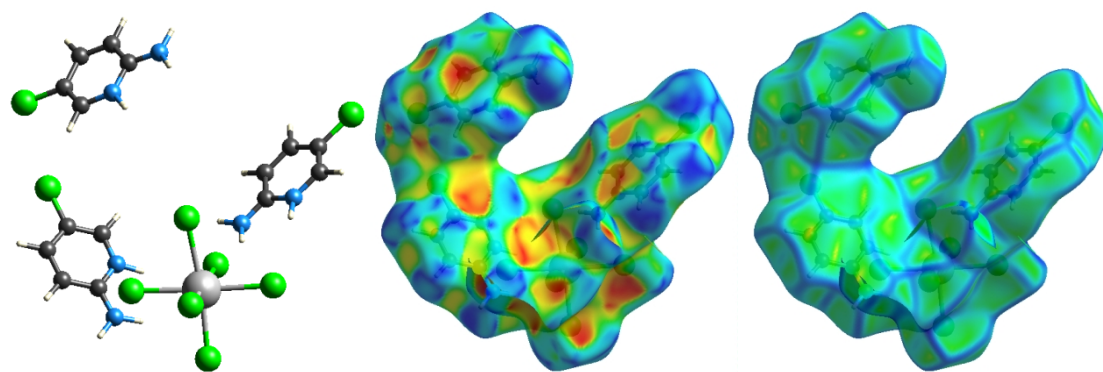


Fig. 7

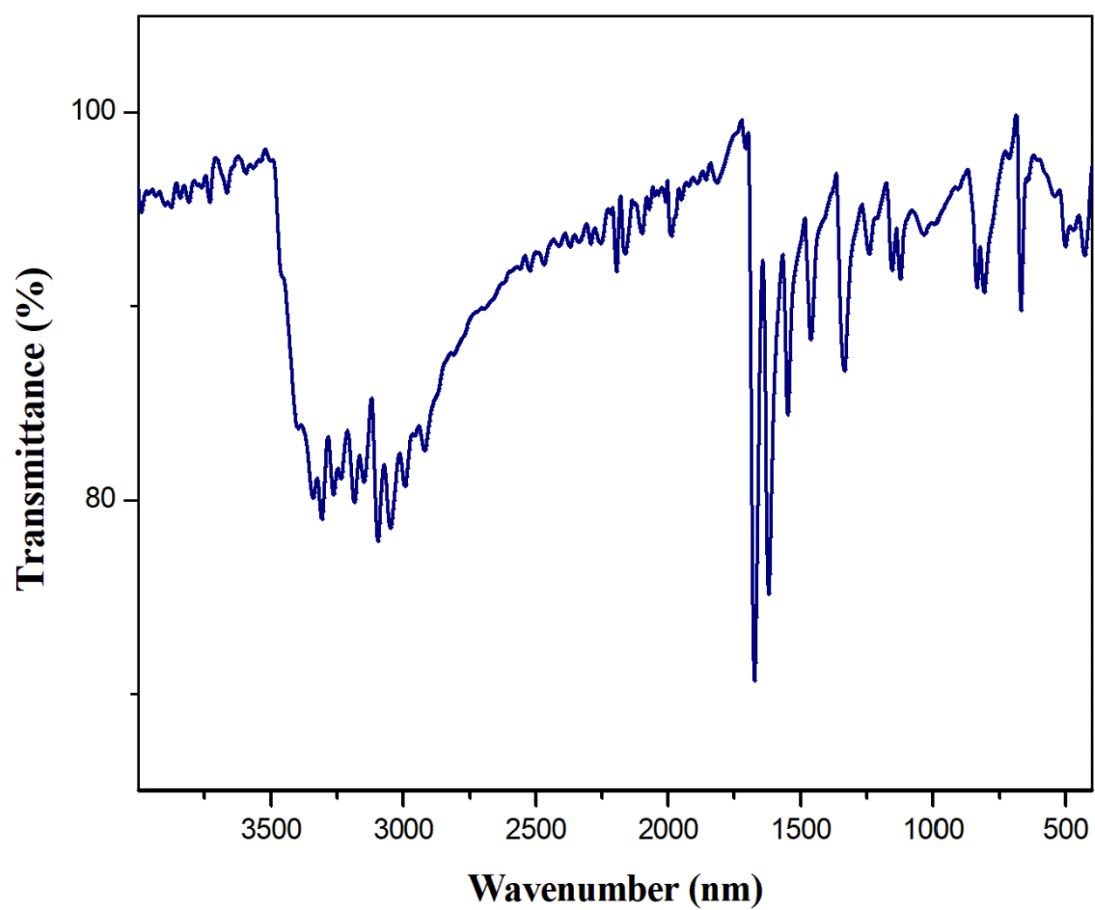


Fig. 8

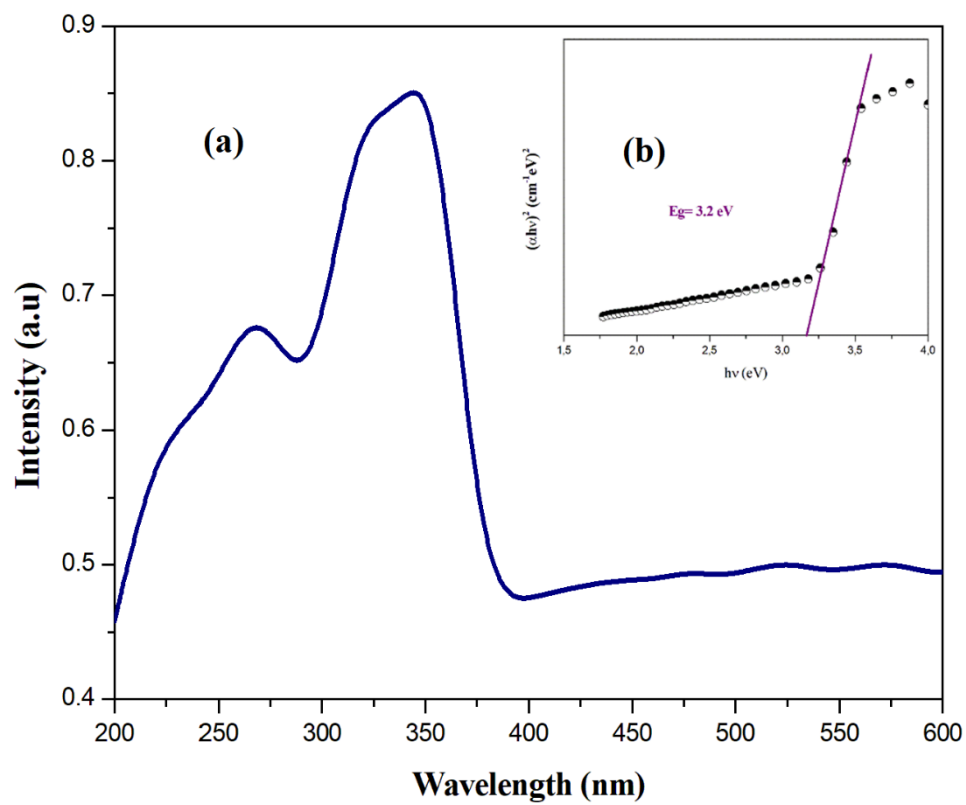


Fig.9

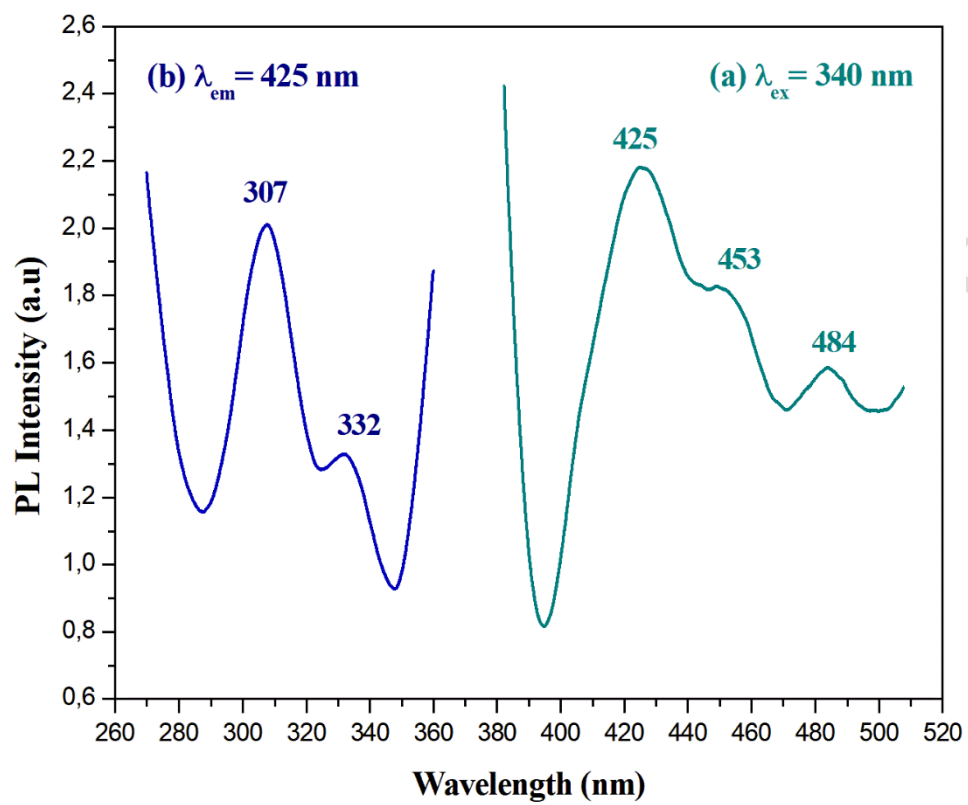


Fig. 10

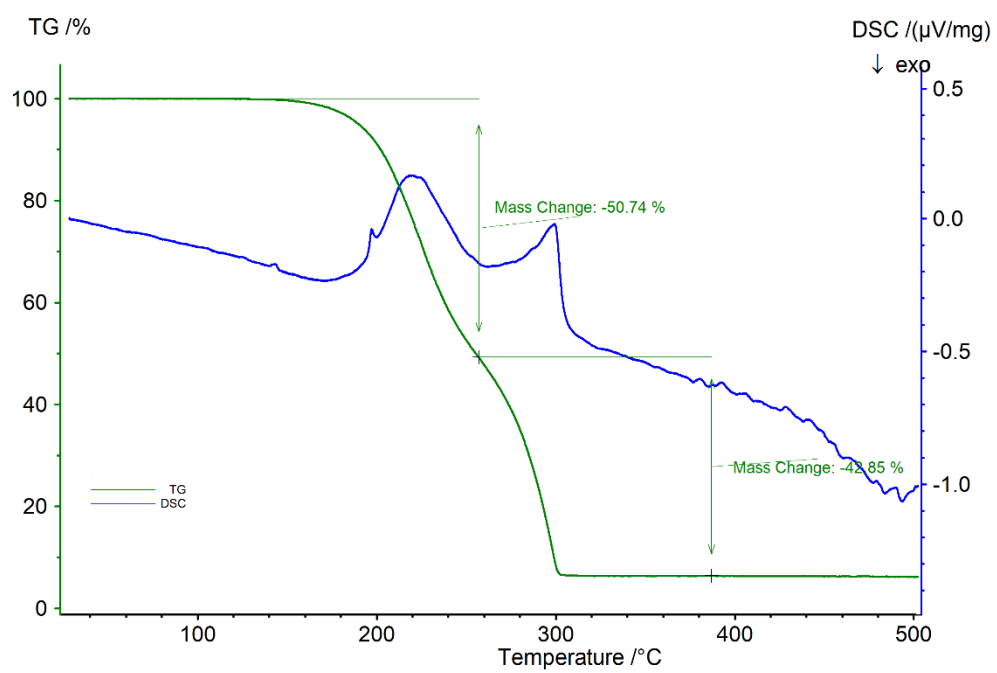


Fig. 11

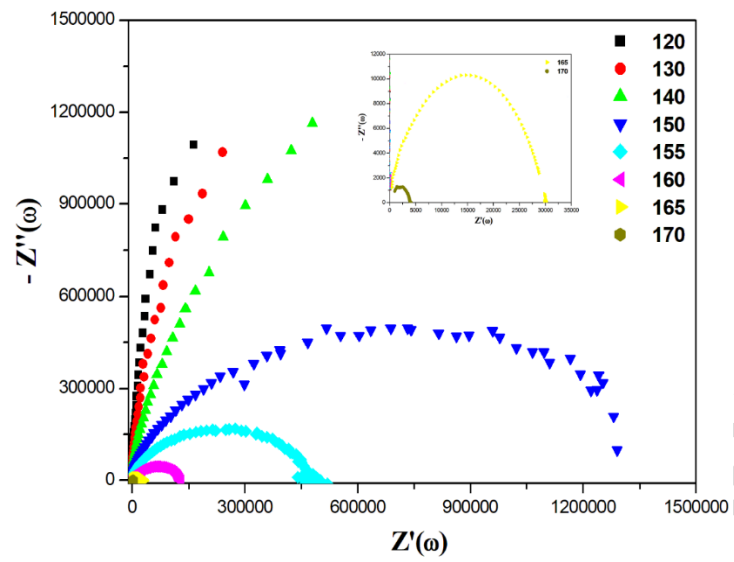


Fig. 12

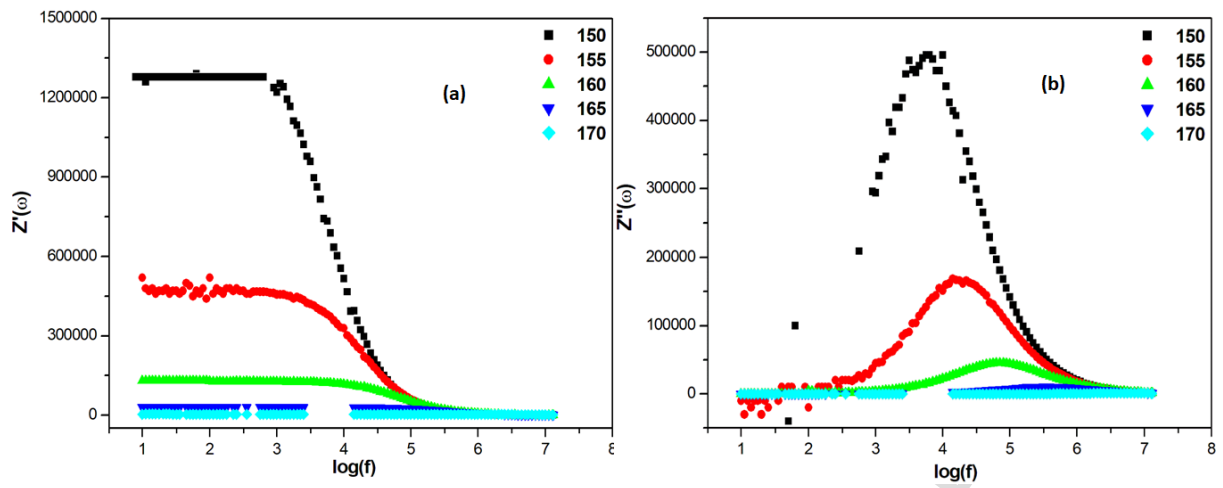


Fig. 13

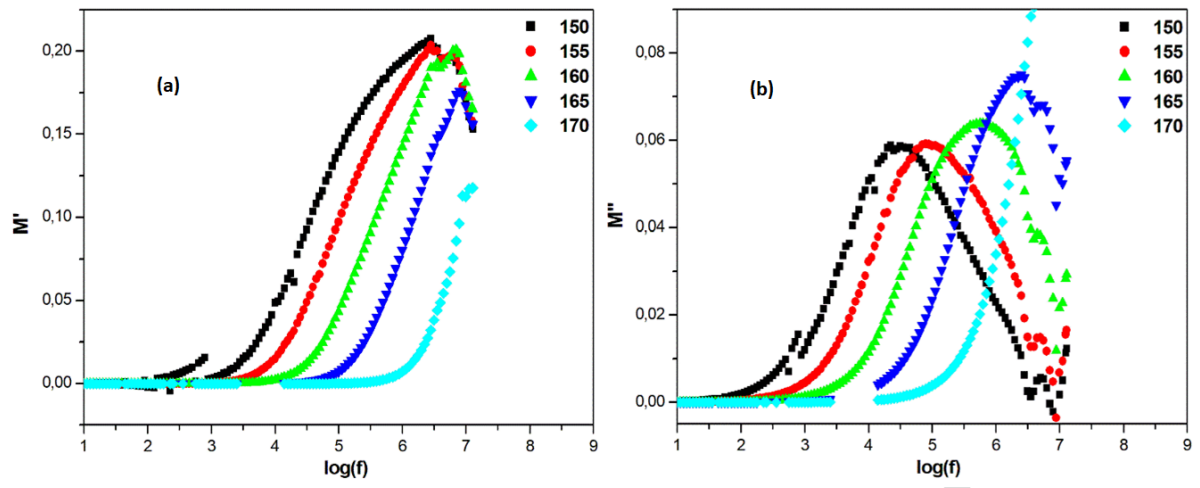


Fig.14

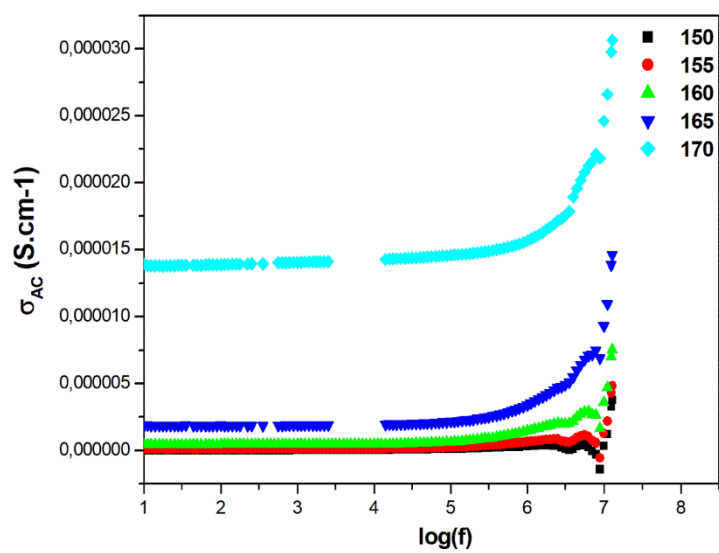


Fig.15

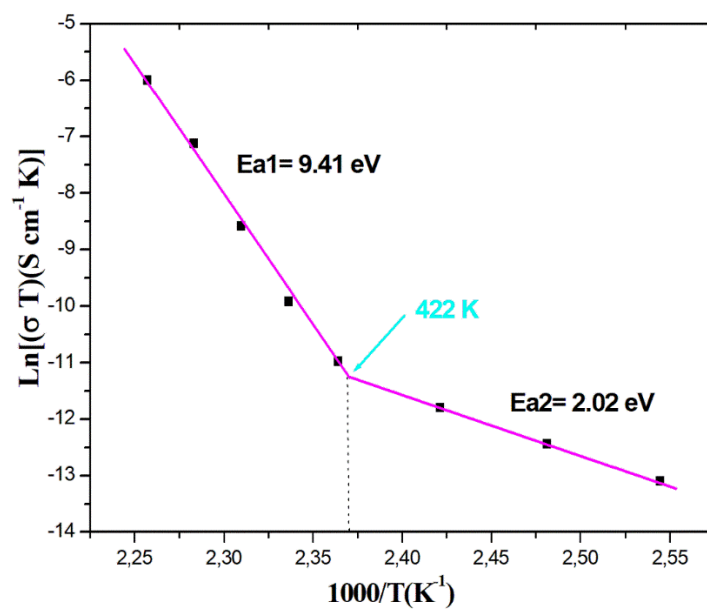


Fig.16

**Highlights**

- The new centrosymmetric compound,  $[\text{C}_3\text{H}_6\text{ClN}_2]_3\text{BiCl}_6$ , was synthesized at room temperature.
- The crystal packing is ensured by  $\text{N}(\text{C})\text{-H}\cdots\text{Cl}$  hydrogen bonds and vdW interactions.
- The compound was examined by IR, UV-visible, fluorescence, TG-DSC, Hirshfeld surface analysis and electrical measurements.